Hindawi
Shock and Vibration
Volume 2023, Article ID 4727706, 19 pages
https://doi.org/10.1155/2023/4727706

Research Article

The Deformation Behavior and Failure Modes of Surrounding Rock after Excavation: A Experimental Study

Jinping Liang,[1,2] **Haoyong Jing**,[3] **Xiaorui Li**,[1,2] **and Gongyu Hou**[4]

[1]*College of Geological Engineering, Institute of Disaster Prevention, Sanhe 065201, Hebei, China*
[2]*Hebei Key Laboratory of Earthquake Disaster Prevention and Risk Assessment, Sanhe 065201, Hebei, China*
[3]*PipeChina Engineering Technology Innovation Co., Ltd., Tianjin 300450, China*
[4]*School of Mechanics and Civil Engineering, China University of Mining and Technology, Beijing 100083, China*

Correspondence should be addressed to Jinping Liang; liangjinping@cidp.edu.cn

Received 31 October 2022; Revised 1 March 2023; Accepted 11 April 2023; Published 6 July 2023

Academic Editor: Denis Benasciutti

The deformation and failure of the surrounding rock during roadway excavation often determine the choice of supporting methods. To study the deformation behavior and failure modes of the surrounding rock after excavation under unloading stress, structural model tests were carried out with a novel experimental device. The present structural model test using partial hollow thick-walled cylinder cement mortar specimen φ200 mm × 280 mm with a horizontal central circular hole of 60 mm diameter and the hollow height of 160 mm was conducted to investigate the deformation, failure characteristics, and AE response of a whole testing process from excavation to postunloading state. Experimental results revealed that the amount of deformation behind the surface is significantly higher than that in front of the surface, and the radial strain increases with the increase of the distance from the surface within the range affected by unloading. Furthermore, the unloading rate has a little effect on the radial deformation of the surrounding rock in front of the surface, but has a substantial effect on the radial deformation behind the excavation surface. The peak value of the strain rate at the unloading rate of 2 MPa/s is much higher than that at the unloading rate of 0.1 MPa/s. According to AE results and the failure of opening the boundary, the increase of unloading rate triggers and exacerbates the damage of the specimen under high in situ stress conditions. The surrounding rock expanded to the inner hollow, accompanied by large dilation and volume changes, and it resulted in the shrinkage of the hole diameter. A large number of rock slices are generated at the opening curved free surface and then fell off, whose morphology is similar to the rock blocks that fell off after caving failure and rock burst in situ field. The results show that the system can accurately simulate the mechanical response and acoustic emission response of the excavated surrounding rock, which provides a new experimental method for further study of the unloading response of the surrounding rock.

1. Introduction

Underground engineering excavation is a dynamic adjustment of the surrounding rock stress in time and space during the process of radial stress unloading, which actually changes from the in situ stress state before excavation to the secondary stress state after excavation. The disturbance process results in the change of the properties of surrounding rocks inevitably. In general, the faster the excavation speed is, the greater the impact on the properties is. Especially in high in situ stress and hard-brittle rock mass [1–3], enormous failure to the underground tunnelling or mining engineering is often caused by excavation unloading, such as large deformation and rock bursts. As a result, it is very important to reduce the influence of disturbance and maintain the stability of surrounding rock by adopting effective measures. Surrounding rock deformation and failure are the most direct reference to the support design [4], but the law and mechanism still remain unclear. Therefore, an in-depth understanding of the deformation laws and failure patterns of surrounding rock is important for the use of effective support design and the determination of reasonable support time.

The excavation face can restrain the surrounding rock deformation around the hole effectively and ensure the implementation of the stability measures behind the

excavation surface. It is considered that rock mass strength, stress level, and plastic radius affect the spatial effect of the excavation face [5–7]. Usually, the spatial effect of the excavation surface is studied by using on-site monitoring convergence displacement. The longitudinal deformation profile (LDP) curve is usually obtained by means of first excavation and then monitoring. The above obtained calculation is complex and the response of the rock mass in front of the excavation face cannot be detected. After excavation, the influence of spatial effect should be considered [8–10]. However, there are few experimental studies considering the spatial effect of the excavation face.

Thick-walled cylinder (TWC) was used to evaluate the roadway stability and is a simple and reliable testing method to study the unloading effect of the roadway excavation [11, 12], which can avoid the influence of the gap effect, complex stress path selection, simulate accurately the hoop effect, and gradient stress around the hollow [13], compared with the traditional true-triaxial unloading test. In recent years, TWC has been widely used in laboratory tests [14–22], theoretical analysis [23, 24], and finite element analysis [25] to study the mechanical response and supporting characteristics of rock mass. For example, Wu et al. compared the influences of different filling materials on the deformation, strength, and failure of TWC sandstone. They concluded that flexible support was the most effective support for the surrounding rock [14]. Wang et al. studied the influences of peripheral compressive stress, aspect ratio, and radial stress gradient on the strength of TWC granite specimens [15]. Zhang et al. and Wu et al. studied the failure form and the generation mechanism of the TWC samples under the condition of pressure unloading in the hole [16, 17].

Acoustic emission (AE) method has been widely used in rock damage fracture and damage localization detection [26, 27]. Zhang et al. conducted the uniaxial multistage loading test on the siltstone, and found that the AE parameters depict the changes in the activity of cracks during rock fracture from temporal perspectives [26]. Dong et al. proposed an AE source location method for structures containing unknown empty areas, which improved the location accuracy [27]. However, the tomography technique in acoustic emission method field also plays an important role in detecting the stress variation and hazard regions in rock mass [28–30]. Dong et al. adopted the 3D tomography method to quantitatively evaluate the six influencing factors of AE wave velocity tomography inversion and proposed a travel time tomography method to identify the buried abnormal regions in complex rock mass structures [28, 29].

The abovementioned work was of great significance to the understanding of the mechanical properties of the rock, but there were few researches on the surrounding rock deformation, fracture, and AE response with different unloading rate. Therefore, we designed a model testing system of roadway excavation unloading and solved the key technical issues of internal and external pressure independent loading and unloading conditions to investigate the response. Then, a series of simulated tunnel excavation unloading tests were conducted with PHTWC cement mortar specimens, and the surrounding rock deformation law, failure mode, and AE response at different unloading rates were obtained. The study provided another way to obtain the mechanical properties and AE response of the roadway surrounding rock.

2. Experimental Methods and Testing System

2.1. Testing Principle. The underground excavation is actually an unloading progress, which is difficult to reproduce through on-site in situ experiments. The underground excavation process of circular sections was simplified into elastoplastic mechanics model, and the mechanical process and the principle of excavation unloading were simulated in a laboratory. The principle is the same as shown in Figure 1. After the "excavated body" being taken out, the stress acting on the "boundary" was dropped to zero, and the surrounding rock shrank and deformed. In the laboratory, the key issues were to achieve the simulation of this unloading process and to study the degree of influence of the unloading rate on the surrounding rock deformation and damage.

2.2. Testing System. The tunnel excavation unloading model testing system for TWC (see Figure 2), which consists of loading system, control system, and data acquisition system, as well as the sealing device, was developed by Hou et al. and other institutions at the Chinese university of mining and technology in Beijing [31]. To solve the key technical issues of internal and external pressure independent loading and unloading conditions for PHTWC, the sealing device was improved, which is expatiated again in Section 2.3.

2.2.1. Loading and Unloading System. Loading and unloading system includes axial loading frame, a moveable pressure chamber, and two superchargers. Axial loading frame adopts an integral structure with great output force of about 3000 KN, as shown in Figure 2(a). Pressure chamber mainly includes sealing device, spherical pressure pad, air outlet, and axial piston unit (see Figure 2(a)). The outer size is 1150 mm (height) × 510 mm (diameter) and the inner size is 526 mm (height) × 350 mm (diameter). The pressure chamber can accommodate TWC specimens with a dimension of 300 mm (height) × 200 mm (diameter). The pressure chamber and the base are clamped by using the load-bearing clamping rings. The base equipped with multiple strain and AE data acquisition channels contains four rollers for moving horizontally on a sliding track. The external cavity supercharger is designed to produce an external confining stress up to 100 MPa, which consists of piston, pressure sensor, and pipeline. The working principle of the internal cavity supercharger is similar to that of the external cavity supercharger (see Figure 2(b)). The testing machine adopts a closed loop full digital measurement and control technology, which is composed of electro-hydraulic servo system, EDC22x measuring controller, a pressure sensor, and a displacement sensor. Test force, displacement, deformation, and extended channel function (e.g., data control, acquisition, display, and

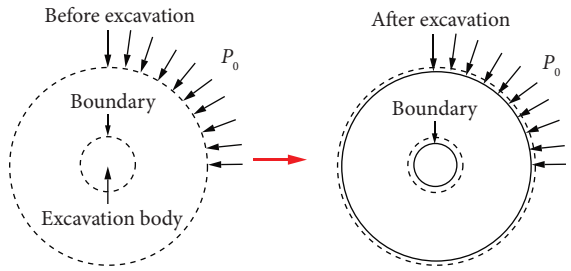

Figure 1: Schematic diagram of real roadway excavation mechanics.

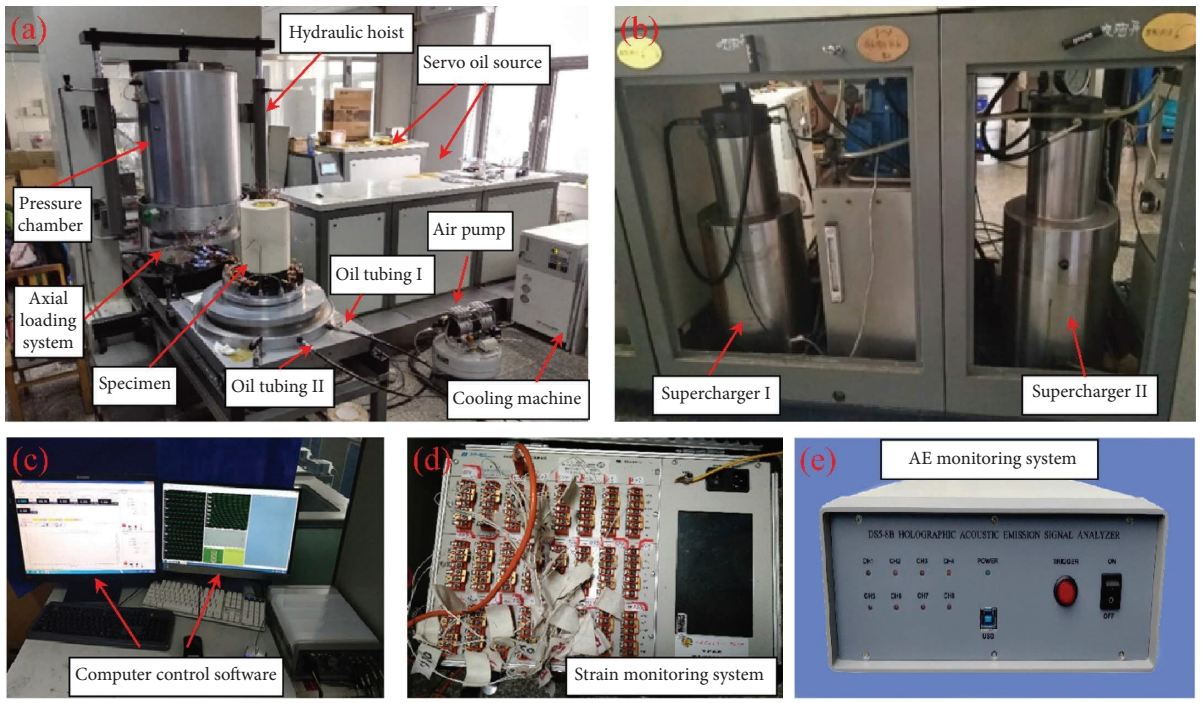

Figure 2: Illustration of the tunnel excavation unloading testing system. (a) The unloading testing machine, (b) the supercharger of internal and external stresses, (c) the computer control software, (d) the strain monitoring system, and (e) the AE monitoring system.

report output) can be managed through the special control software (see Figure 2(c)).

2.2.2. Data Acquisition System. Loading and unloading data, strain data, and acoustic emission data are collected through the data acquisition system. PCI acquisition card is used to collect data obtained from the pressure sensor and the displacement sensor. The data storage paths and parameters can be set in the computer control system software. Strain gages were arranged to collect real-time strain data. A twenty-four channels static strain meter (see Figure 2(d)) (model: DH3818Y), equipped with $\Sigma - \Delta A/D$ analog-to-digital converter, measuring range from $-30000\,\mu\varepsilon$ to $+30000\,\mu\varepsilon$, can realize the dynamic and static continuous accurate data acquisition. Uninterrupted power supply of the battery can avoid the influence of AC power on AE collection during testing. An all-information AE signal analyzer (model: DS5-8B) (see Figure 2(e)) can record the waveform and information state of 8 channels synchronously. Using supporting AE analysis software, the setting of the storage path and collection parameters is realized. Considering that the AE results could be affected by noise, the testing machine and AE equipment were grounded, and the sensor and testing machine joints were connected with shielded wire to reduce the interference of an external magnetic field on AE signals. At the same time, the anthropogenic and external noise during testing should be avoided.

2.3. Experimental Sealing Device. As shown in Figure 3, the sealing device is mainly composed of bottom sealing block, top gasket block, top sealing block, fixed steel rod, rubber membranes, and pressure bending pipes.

2.3.1. Loading Block. Bottom sealing block is a horizontal solid cylinder with grooves (see Figure 3(a)) for sealing the outer rubber membrane. Data lines past through the sealing block to realize the data transmission. One end was connected to the specimen, and the other end was pulled out

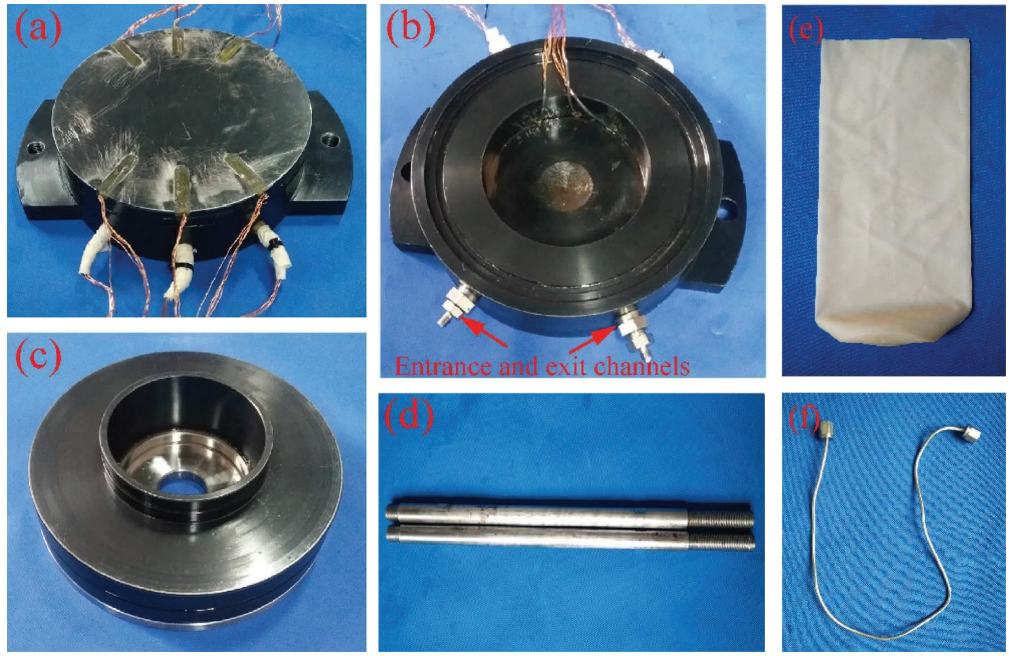

Figure 3: Sealing device: (a) bottom sealing block, (b) top gasket block, (c) top sealing block, (d) fixed steel rods, (e) rubber in the hole, and (f) pressurized pipe.

through the high-voltage resistance terminal and connected to the base joints. Top gasket block (see Figure 3(b)) contains two grooves in the side wall, which are, respectively, used to seal the outer and inner rubber film. A 10 mm thick steel gasket was attached below the top block, which could be removed and replaced to change the hole size required for testing needs. The top sealing (see Figure 3(c)) is a key to achieve inner stress loading and unloading. Two oil holes were designed on the top sealing block for entering and exiting the silicone oil, thus ensuring that the cavity of the specimen could be filled with oil. The O-ring was sealed in a groove, which prevented the oil from passing through each other under axial pressure and ensured the success of loading and unloading. Similar to the bottom sealing block, the top sealing block also contains a data cable that can be used as an expansion channel.

2.3.2. Rubber. The success of the testing is closely related to the isolation of internal and external cavities. The combination of elastic rubber film and rubber isolates the inner and outer chambers. One reason is that it can well isolate the oil in the internal and external cavities. Another reason is that it has great elasticity and can still tighten and seal with the deformation of the specimen.

2.3.3. Fixed Steel Rods and Pressurized Pipes. Fixed steel rod (see Figure 3(d)) is made of high-quality and high-strength steel with threads engraved at both ends. Two symmetrically distributed solid steel rods could fix the specimen in the sealing device and prevent the specimen from moving under external forces such as buoyancy of oil, resulting in axial bias.

Pressurized pipe is a part that connects the oil port on the top sealing block to the inner cavity filling tube. It must be able to resist large confining pressure and ensure the joints do not leak.

2.3.4. Working Principle of the Load-Unload State. Figure 4 is a sealing device assembly diagram; the assembly process is as follows: first, the bottom sealing block, the specimen of the inner and outer rubber (closed end facing down and opening end facing upward), top gasket, and top sealing block were placed horizontally in turn. Next, the data lines on the specimen were connected to the testing device, and the connectivity was detected by strain gauge. Then, the inner and outer rubber films were fixed on the top block and the bottom sealing block, respectively. Finally, the pressurized pipes were connected and two steel rods were fixed. The acoustic emission sensors were installed on the premarked position.

The sealing device separates the inner and outer chambers effectively. The testing system combined with the sealing device realized the independent loading and unloading control of the axial, internal, and external confining of the specimen. The loading and unloading system can control the axial pressure and the external cavity supercharger and internal cavity supercharger can control the external and internal pressure independently of each other. Before the testing, the internal and external cavities of specimens were filled with silicone oil, and the servo valve was controlled by the controller to act on the supercharger to realize the independent loading and unloading of internal and external confining stresses.

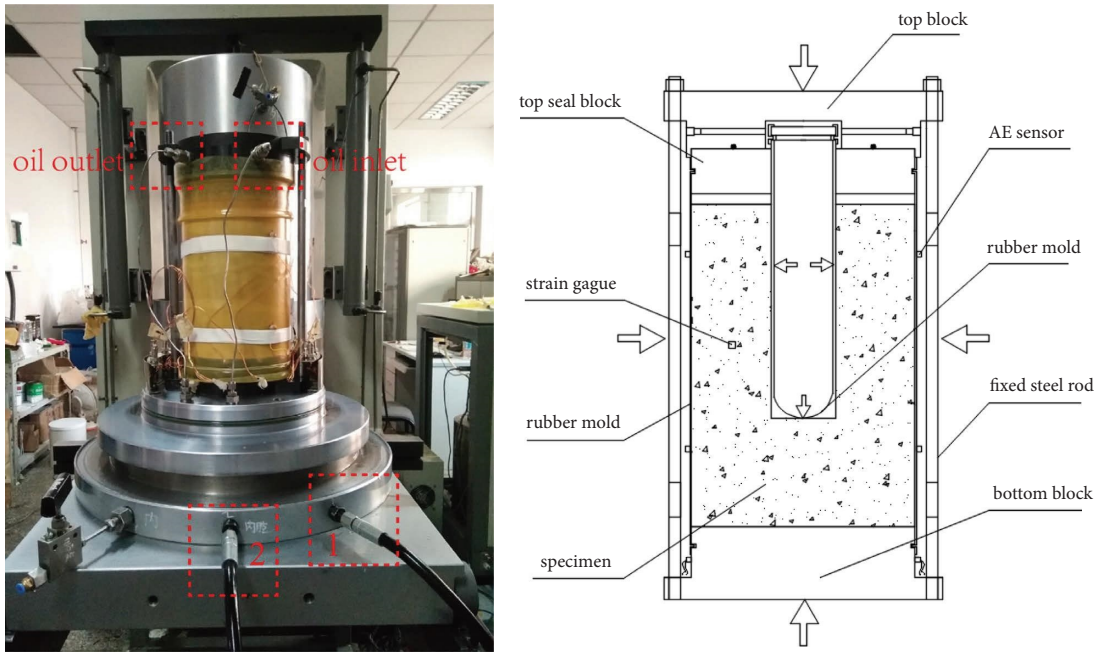

Figure 4: Installation diagram of the sealing device.

2.4. Specimen Preparation. Cement mortar materials, namely, rock-like materials, characterized by obtained easily, good stability, and moldability, using to simulate the mechanical properties well of rock materials, were used in the experimental research widely [32–34]. By adjusting the mixing proportion of the cement mortar, standard core specimens similar to mechanical properties of sandstone were obtained [35]; the physical and mechanical parameters of the cement mortar and sandstone are shown in Table 1. Hence, cement mortar materials with the same proportion as core specimens were selected to make PHTWC for testing (see Figure 5(a)).

The specimen size mainly considers the following two points. (a) Size suitability: The reduction of hole diameter will lead to significant strength effect and structural effect of the specimen. This phenomenon is more pronounced when the hole diameter is less than 50 mm. As a result, the stress value required for the failure of the inner wall of the hole increases significantly. In fact, the section size in practical engineering is large, and the influence of strength effect and structural effect is not obvious. This results in a big discrepancy between the testing results and the actual situation [36]. (b) Boundary effect: After excavation unloading in roadway construction, the influence range of surrounding rock stress disturbance is about 3~5 times the hole diameter. In order to eliminate the boundary effect, the outer diameter of the model testing specimen was selected as 3~5 times the hole diameter. As a result, the dimensions of PHTWC are as follows: the outer size is 280 mm (height) × 200 mm (outside diameter) × 60 mm (inside diameter), the hollow height is 160 mm, and the solid height is 120 mm (see Figures 5(a) and 6). Specimen processing accuracy is in strict accordance with the standards of the international association of rock mechanics.

Table 1: Mechanical and physical parameters of cement mortar material and sandstone.

Rock type	CS (MPa)	E (GPa)	ν	ρ ($g \cdot cm^{-3}$)
Cement mortar	25.0	10.2	0.19	1.97
Sandstone	20~170	4.9~78.5	0.02~0.2	2.1

Six AE sensors (model RS-5A, operating frequency range from 50 kHz to 100 kHz), withstand high oil pressure, mounted on the outer wall of the specimen (see Figures 5(b) and 5(c)), were used to acquire AE signals. The sampling rate and the trigger threshold of the AE were set to 3 MHz/s and 30 dB, respectively. The silicon grease, as coupling agent, can reduce the signal attenuation and enhance the signal transmission between the specimen and the sensors. Eight strain gages (no. from #1 to #8), with the fence length size of 5 mm × 3 mm, sensitivity factor of 2.08 ± 0.5%, and resistance value of 120 ± 0.3 Ω, were distributed in different positions inside the specimen as shown in Figure 6. Strain gauges attached in a very fine and sparse wire (0.2 mm) mesh were pre-embedded in the cement mortar. Wire mesh and cement mortar materials have a similar linear expansion coefficient and good adhesion, so that they can be deformed together during testing. In addition, the wire mesh does not affect the mechanical behavior of the specimen in the high-stress testing environment.

2.5. Testing Design. A load of same magnitude was applied to the axial, inner, and outer of specimens, i.e., as shown in Figure 7. After the loading strain was stable, external confining stress and axial stress were kept, and the internal confining stress was relieved at different rates, so as to simulate the excavation unloading process of roadway.

(a) (b) (c)

Figure 5: (a) Overview of the cement mortar specimens in the study. (b, c) Positions of the AE sensors.

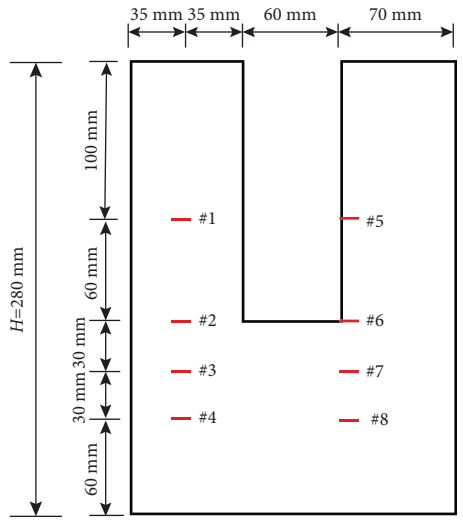

Figure 6: Strain gages layout diagram of PHTWC specimen.

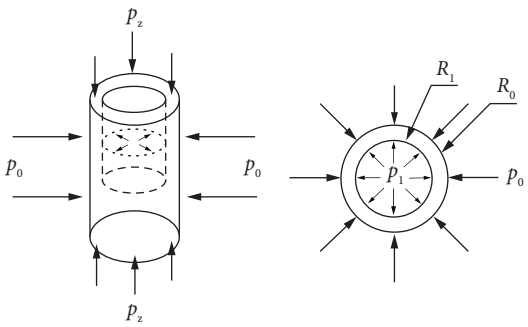

Figure 7: Schematic of initial stress of PHTWC specimen.

Before the test, the specimen was placed in the sealing device, and the tightness was check. The pressure chamber was installed and the monitoring equipment was debugged. The test procedure included the following three steps:

(1) The experiment paths are as shown in Figure 8. First, axial stress was applied to 2.5 MPa at a constant loading rate of 0.1 MPa/s to prevent the specimen to move during silicone oil filling process. After that, the external and internal confining stresses were added to 2.5 MPa at the same loading rate (0.1 MPa/s) as the axial stress.

(2) Then, the axial stress, external, and internal confining stresses were increased to the designed levels at a constant loading rate of 0.1 MPa/s, using the experimental paths plotted in Figure 8. To simulate the stress state of the original rock, the deformation was kept stable for 10 min after loading.

(3) Finally, the internal confining stress was relieved under stress control mode, and the difference of external stress and internal stress (hereafter called deviatoric stress) continues to increase. There are two unloading rates: 0.1 MPa/s and 2 MPa/s. To obtain the mechanical response of surrounding rock after unloading, the deformation was kept stable for 8 min.

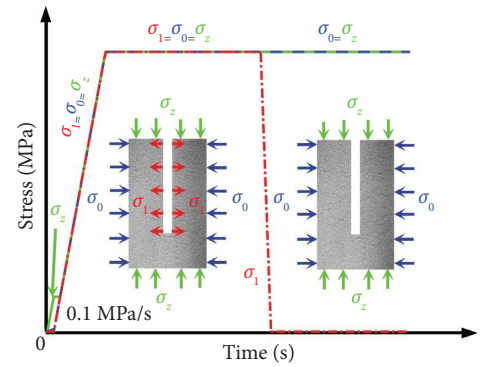

Figure 8: Loading and unloading paths and stress combinations for the experimental process, where σ_1 is the internal confining stress, σ_0 is the external confining stress, and σ_z is the axial stress.

The axial stress, internal confining stress, and external confining stress were automatically recorded by computer control system software, and the recording speed is 16 times per second. Meanwhile, the strain changes and AE signals were monitored at the point in real time by strain monitoring system and AE monitoring system, respectively.

3. Experimental Results

3.1. Influence of Unloading Rate on Deformation. Figure 9 shows the radial strain response and cumulative AE hits curves of different measuring points from the unloading tests for specimens with the unloading rates, i.e., 2 MPa/s and 0.1 MPa/s. As presented in Figure 9, rock mass ahead of the excavation face has produced slight deformation under the influence of excavation unloading effect. At the position of 1 times the hole diameter in front of excavation (Figure 9(a), gage #7), the radial strain of surrounding rock presented tension-compression alternations, while compression appeared at 2 times the hole diameter (Figures 9(a) and 9(b), gage #8). This phenomenon may be caused by the intensity of stress adjustment and the mechanical properties of surrounding rocks after unloading.

Unlike the strain characteristics of the surrounding rock ahead of the excavation face, the radial tensile strain behind the excavation face was relatively large. The deformation of the surrounding rock varies with different spatial positions, such as longitudinal position and radial depth. Although the spatial positions were different, the evolution characteristics of the radial strain were similar for the same unloading rates. In the process of internal confining stress unloading, the radial tensile strain at or near the inner wall rock was produced rapidly. Especially when the unloading rate was 2 MPa/s, the slope of the radial strain curves was highly big (Figure 9(a)). After unloading, the growth rate slows down. In the end, when the radial depth was constant, the radial strain value was the largest at the distance from excavation face of 2 times the hole diameter. For example, the measuring point strain values of gage #5 and gage #1 were greater than those of gage #6 and gage #2, respectively. Within the influence range of excavation unloading in this study, when the radial depth was constant, the greater the longitudinal distance from the excavation face was, the greater the radial deformation was, which has also been observed by other researchers [6]. When the longitudinal position was constant, the radial strain of inner wall rock was higher than that at the radial depth of 35 mm from the inner wall. For instance, the measuring point strain values of gage #5 and gage #6 were larger than those of gage #1 and gage #2, respectively. This shows that the inner wall rock might be more susceptible to the condition of excavation. In addition, the radial strain agrees with the cumulative AE hits in Figure 9.

Figure 10 shows the deviatoric stress-strain curves from two unloading rates during the unloading process. With the increase of the deviatoric stress, at unloading rates of 2 MPa/s, the stress-strain curves presented a trend of convergence. However, when the unloading rate was 0.1 MPa/s, the trend of the stress-strain curves was developmental. During the unloading process, radial strain rate continues change with the increase of deviatoric stress. The influence of two unloading rate in this study on radial strain rate is discussed in Section 3.2.

Figure 11 shows the radial strain variation rules of eight measuring points under two unloading rates. The variation trend of the curve reflects the deformation of surrounding rock at different locations away from the face due to the excavation unloading effect. The results show that there is an obvious spatial effect during the unloading process, which was consistent with the research results of Zhao et al. [37]. It can be found that the surrounding rocks at different locations are affected by the unloading effect to different degrees. At 1~2 times the hole diameter before the excavation, the surrounding rock on the cave wall or at the radial depth of 35 mm from the cave wall has been slightly deformed. The surrounding rocks in this range were not affected by the unloading rate, and the resulting radial response variable was essentially the same. The deformation of the surrounding rock within the diameter of 0 to 1 times hole in front of the excavation increased significantly in the process of approaching the excavation surface. In addition, the surrounding rock at the radial depth of 35 mm from the carve wall was affected by unloading rates. Although the surrounding rock at the cave wall is greatly deformed by the impact of unloading, it is still not affected by the unloading rate.

The surrounding rock excavated at 1~2 times the hole diameter behind the excavation surface lost its radial support force and released a large deformation to the excavation surface. The excavation spatial effect of the surrounding rock far away from the excavation surface was reduced, and the sufficient release of stress resulted in an increase in deformation. Studies have shown that the surrounding rock deformation was related to the spatial effect of the excavation surface. In other words, the more significant the effect was, the smaller the radial deformation was. The testing results show that the spatial effect of two different unloading rates was different in the surrounding rock at different radial depths. Different unloading rates had different spatial effects on surrounding rocks at different radial depths. The surrounding rock at the radial depth of 35 mm from the cave wall was continuously affected by the unloading rate, and the radial deformation of the rapid unloading was less than the radial deformation of the slow unloading at the same distance from the excavation surface. Hence, the effect of the surrounding rock at the radial depth of 35 mm from the inner wall was more obvious, when the unloading rate was 2 MPa/s. However, the inner wall rock was more obvious, when unloading rate was 0.1 MPa/s. This is an interesting finding, and whether it is related to other factors remains to be studied.

3.2. Influence of Unloading Rate on Strain Rate. The strain increment per unit time is defined as the strain rate, which can be written as follows:

$$\dot{\varepsilon}_r = \frac{(\varepsilon_r - \varepsilon_r')}{\Delta t}, \tag{1}$$

where ε_r is radial strain and $\dot{\varepsilon}_r$ is radial strain rate. The larger the strain rate, the faster the deformation per unit time.

Figure 12 shows the radial strain rate evolution of four measuring points (gages #3, #4, #7, and #8) ahead of the excavation face, during the unloading and maintenance stage. The radial strain rate varies steadily around 0 value ahead of the excavation face, during the two unloading rates

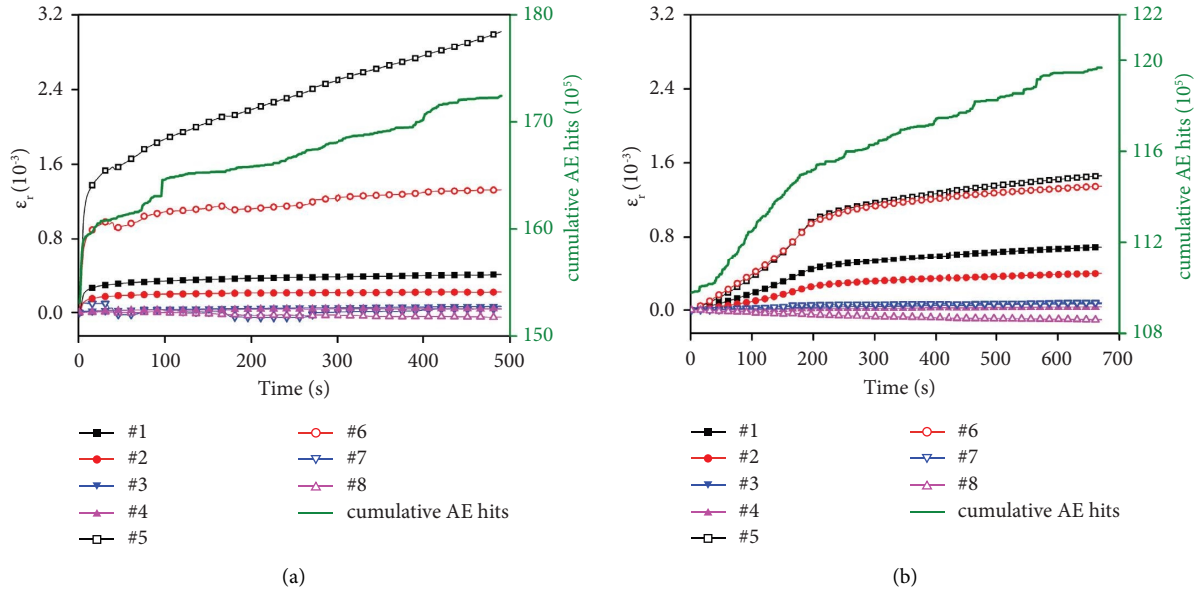

FIGURE 9: Radial strain response and cumulative AE hits curves of different measuring points for specimens with the unloading rates of (a) 2 MPa/s and (b) 0.1 MPa/s under initial confining stress of 20 MPa. Note: (a) lasted 10 s in the unloading stage and (b) lasted 200 s in the unloading stage. Both of them lasted 480 s in the maintenance stage.

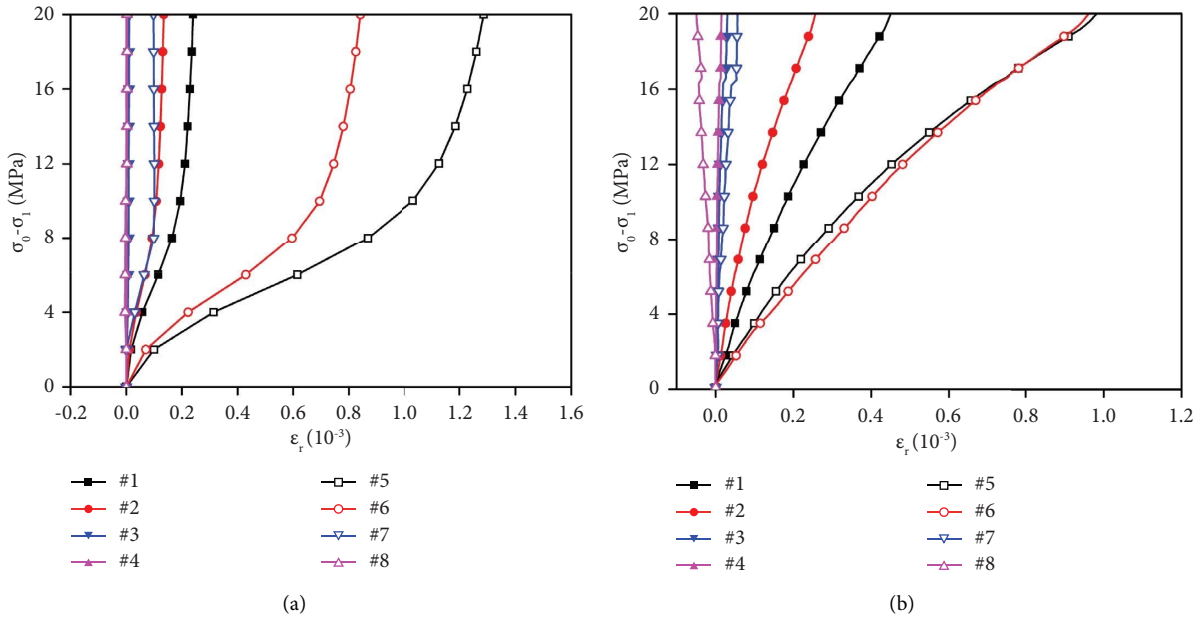

FIGURE 10: Radial deviatoric stress-strain curves of different measuring points for specimens with the unloading rates of (a) 2 MPa/s and (b) 0.1 MPa/s under initial confining stress of 20 MPa during unloading process. Note: (a) lasted 10 s in the unloading stage and (b) lasted 200 s in the unloading stage.

in this study. Moreover, the radial strain rate was higher as a whole at the unloading rate of 2 MPa/s. When the unloading rate was 0.1 MPa/s, note that three points with high strain rate appeared by accident at the later stage of unloading, which may be related to the instant dislocation of positions between particles caused by the expansion of internal cracks in the specimen itself.

In general, at the position of 1~2 times the hole diameter ahead of the excavation face, the radial strain rate of the surrounding rocks was very small, and the value was basically the same even if the unloading rate was different. Therefore, it is considered that the unloading rate has little effect on the radial deformation velocity of surrounding rock outside the 1 times the hole diameter.

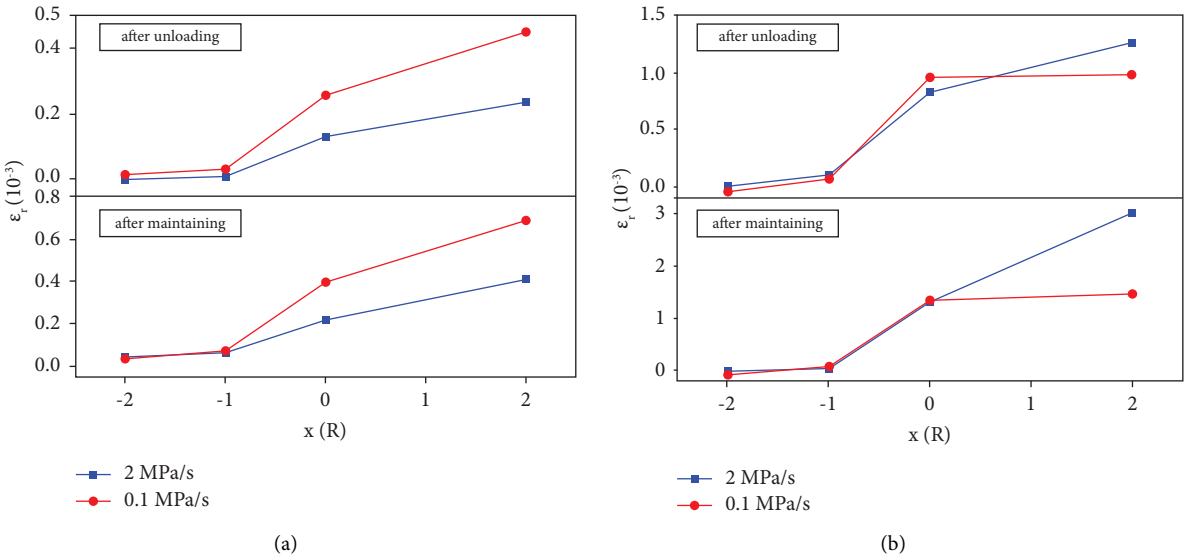

Figure 11: Radial strain law of the surrounding rock at different distances from the excavation face. Note: x is the distance from the excavation face and R is the excavation radius. x/R ratios behind the excavation face equate to positive values. x/R ratios ahead of the excavation face equate to negative values. (a) Surrounding rock at a radial depth of 35 mm from the inner wall and (b) surrounding rock at the inner wall.

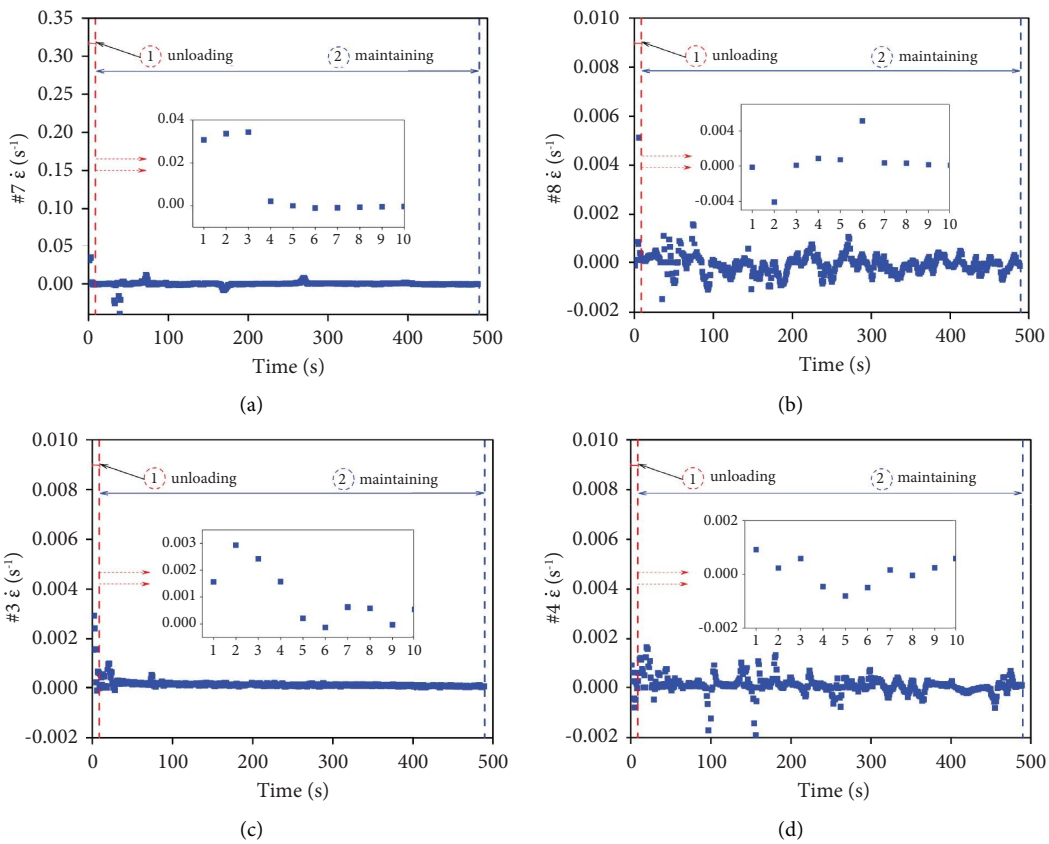

Figure 12: Continued.

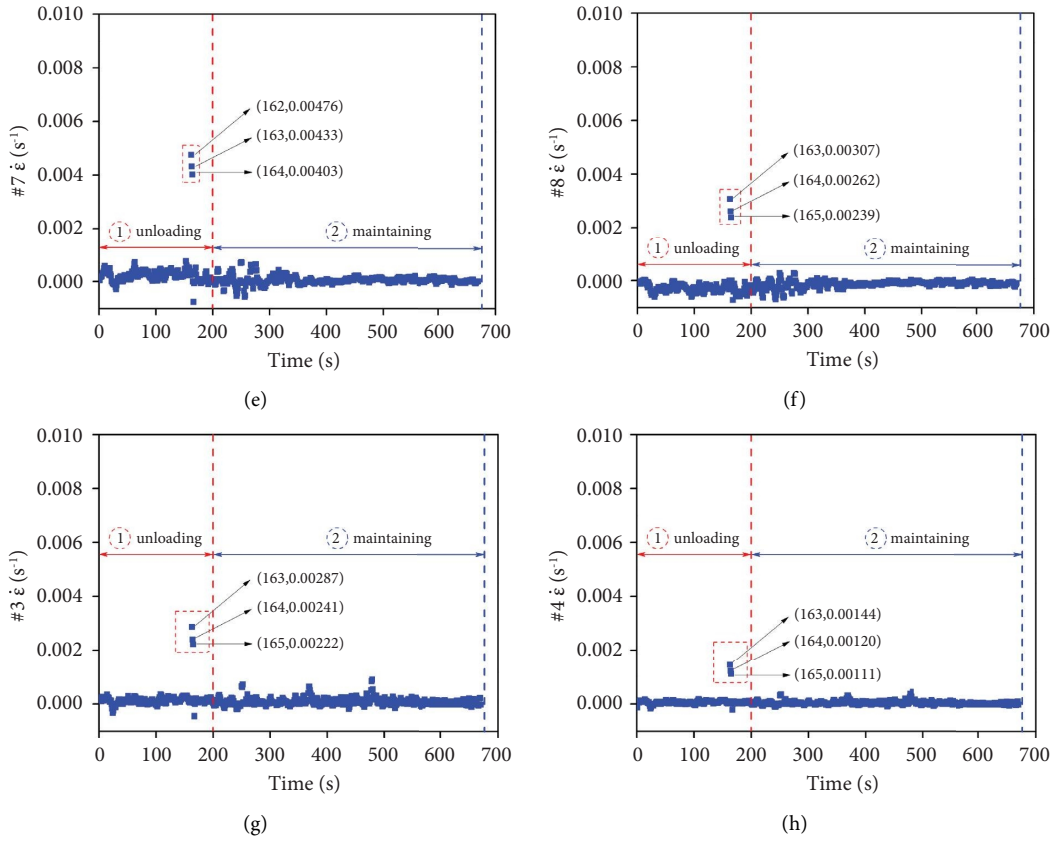

Figure 12: Radial strain rate of four measuring points ahead of the excavation face from the unloading tests for specimens with the unloading rates of (a–d) 2 MPa/s and (e–h) 0.1 MPa/s under initial confining stress of 20 MPa. Note: (a–d) lasted 10 s in the unloading stage and (e–h) lasted 200 s in the unloading stage. Both of them lasted 480 s in the maintenance stage.

Figure 13 shows the evolution and the goodness fitting (R^2) curves of radial strain rate for four measuring points (gages #1, #2, #5, and #6) behind the excavation face, during the unloading and maintenance stage. At the inner wall, the peak strain rate of the surrounding rock was higher than that of the radial depth of 35 mm from the inner wall, such as the measuring point strain value of gage #5 and gage #6 which were larger than that of gage #1 and gage #2, respectively. It also can be found that the radial strain rate increased first and then decreased gradually, during the unloading and maintenance stage of the two unloading rates in this study. When the unloading rate was 2 MPa/s, the fitting curves of strain rate can be divided into two sections. The strain rate increased linearly, and reached a peak when the stress was relieved to 30% of the initial confining stress, and then decreased exponentially and stabilizes around 0 value. However, the fitting curves of the strain rate can be divided into three sections, when the unloading rate was 0.1 MPa/s. The strain rate increased linearly, then exponentially reached the peak when the stress was discharged to 94% of initial confining stress, and finally decreased exponentially and stabilized around 0 value. The peak value of the strain rate at the unloading rate of 2 MPa/s was much higher than that at the unloading rate of 0.1 MPa/s. This phenomenon was more obvious at the inner wall rock. The influence mechanism of the unloading rate on radial strain rate is discussed in Section 4.1.

3.3. Influence of Unloading Rate on Failure Pattern. Figure 14 shows the photographs of the specimens after unloading testing. It is clearly seen that failure behaviors were triggered by a relatively high deviatoric stress. When the deviatoric stress increased to 20 MPa, there was no macroscopic damage on the specimen (Figures 14(a) and 14(b)). When it increased to 30 MPa, the surrounding rock was squeezed towards the opening apparently, accompanied with large dilation and volume changes. A large amount of rock slab and rock slices peeled off from the inner wall (Figures 14(c) and 14(d)). These fragments were collected and presented in Figure 14(f), characterized by thinner edges and a thicker middle section, produced at the opening curved free surface and then fell off. Note that abundant powders remained on the curve free surface or fell off, which can be explained to strong friction between the particles during rock flake peeling. This phenomenon, which has also been observed by other researchers [40], was similar to the rock blocks that fell off after caving failure and rock burst in situ field. By comparison, it is easily found that the fracture behavior of the specimen in the simulated testing was similar to the thin wedge bodies generated by rock burst damage (Figure 14(e)) and bulge deformation of surrounding rocks generated on the roadway wall in the field (Figure 14(h)). In addition, the failure was more violent, and the rock fragments at inner wall were appeared with larger

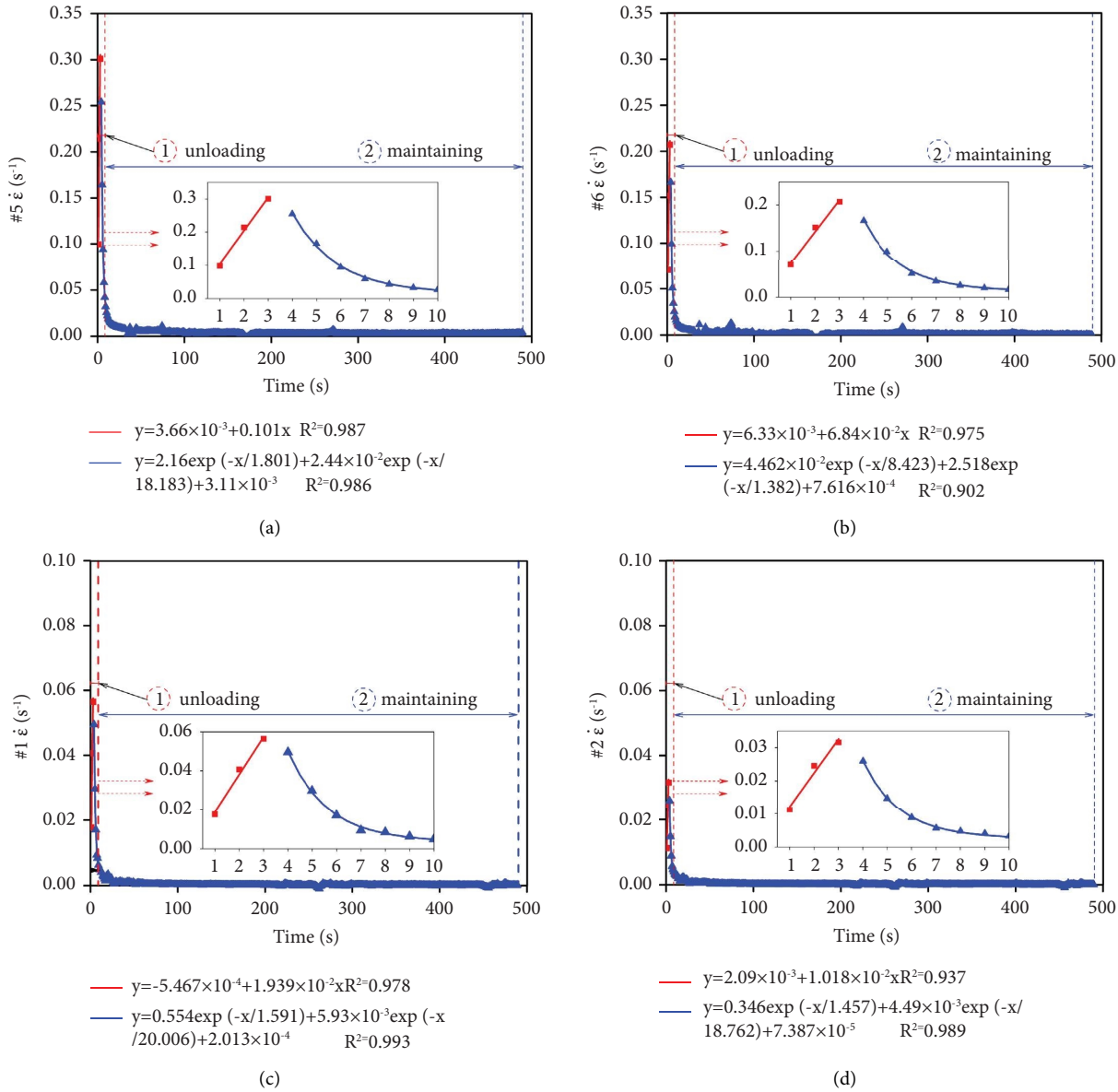

Figure 13: Continued.

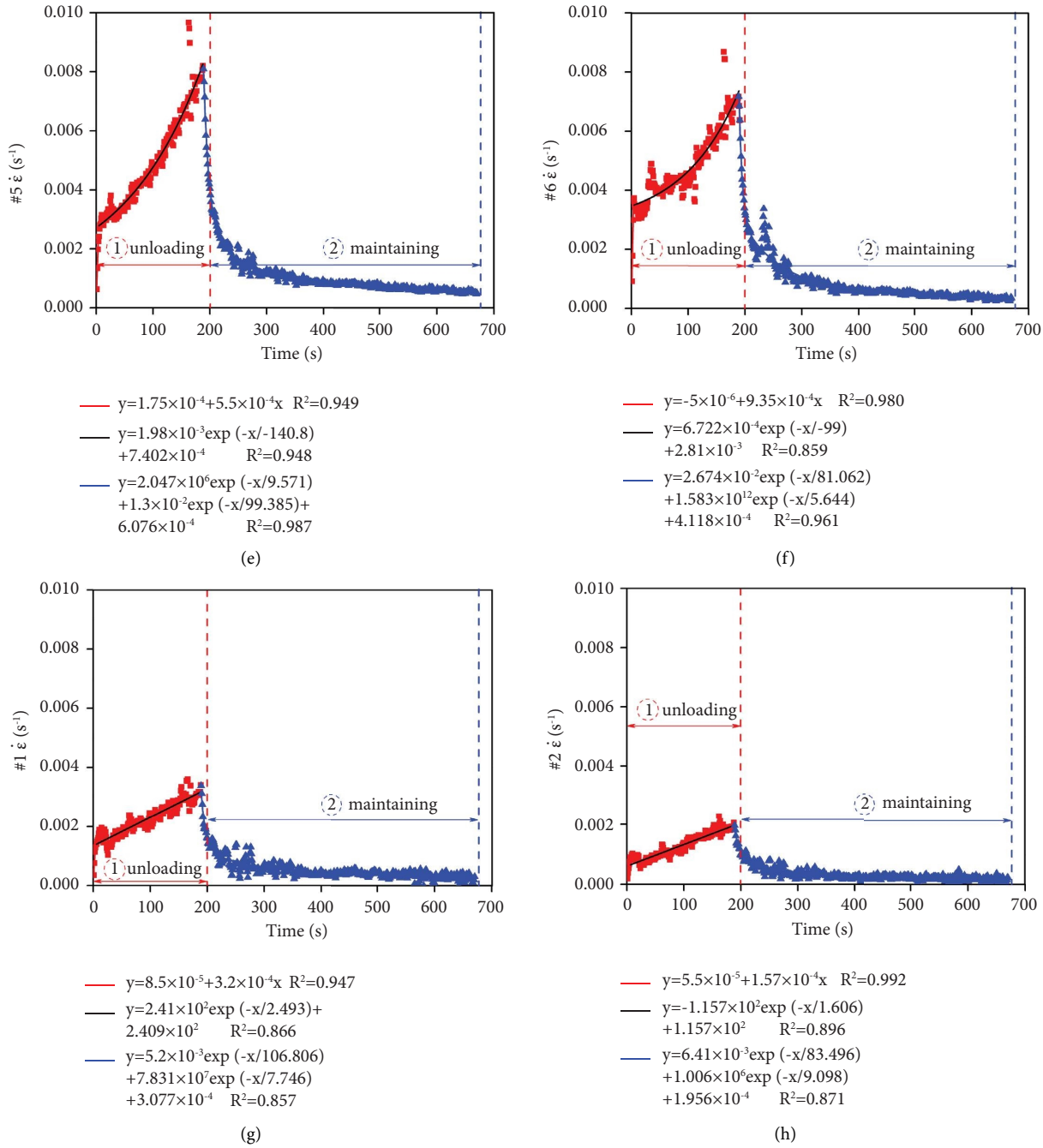

Figure 13: Radial strain rate of four measuring points behind the excavation face from the unloading tests for specimens with the unloading rates of (a–d) 2 MPa/s and (e–h) 0.1 MPa/s under initial confining stress of 20 MPa. Note: (a–d) lasted 10 s in the unloading stage and (e–h) lasted 200 s in the unloading stage. Both of them lasted 480 s in the maintenance stage.

volume (Figure 14(g)), at the unloading rate of 2 MPa/s. Zhao et al. investigated that, the failure mode of rectangular prismatic granite specimen showed a transition from strain bursting to spalling during the true-triaxial unloading process, at the unloading rate of 0.05 MPa/s. When the deviatoric stress was induced to 0.025 MPa/s, the rock failure was dominated by spalling [41]. Unfortunately, in this study, we were unable to acquire the visualization of cracking during unloading, because the high-speed camera cannot be used in oil. So, the AE was adopted to investigate the failure mechanism and damage intensity of the specimens at two unloading rates in Section 3.4.

3.4. Influence of Unloading Rate on AE Characteristics. Figure 15 shows the characteristic of the AE hits during the whole test which included the following four stages: initial loading stage, maintenance stage, unloading stage, and maintenance stage after unloading. (a) In the initial loading stage, AE hits experienced a steady increase under the

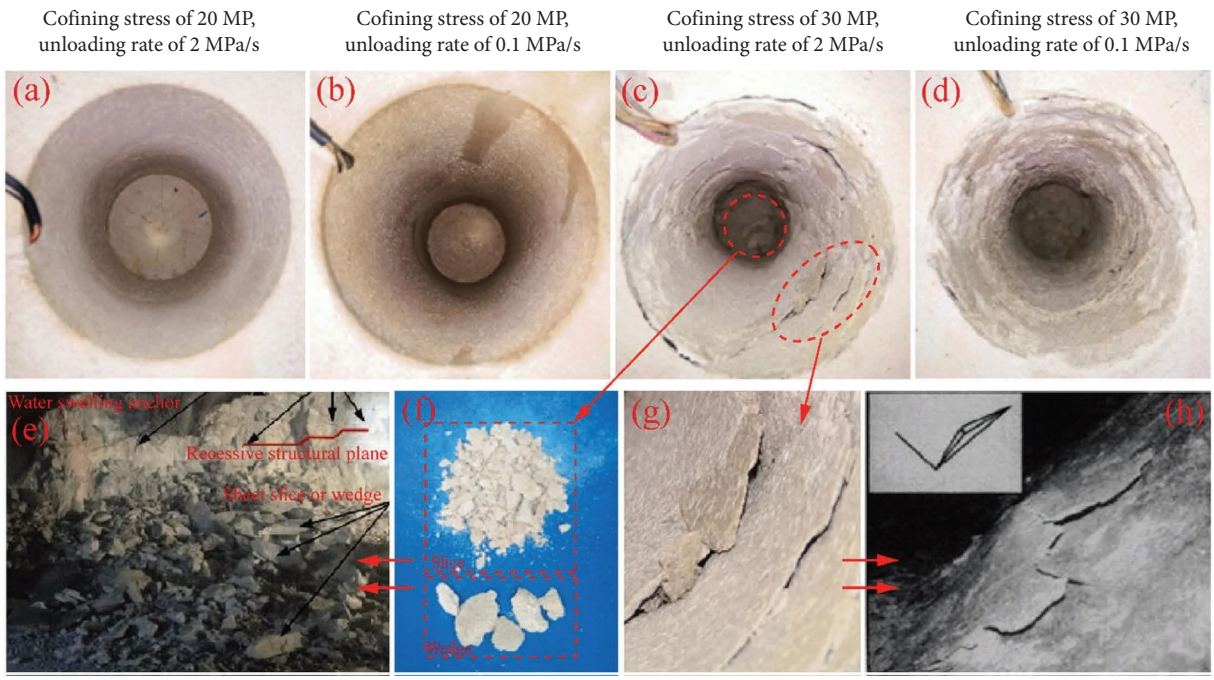

Figure 14: (a–d) Photographs of the inner wall with the unloading rates of 2 MPa/s and 0.1 MPa/s under initial confining stress of 20 MPa and 30 MPa. Comparison of failure fragments in the field and tests: (e) rockburst fragments of Jinping hydropower station [38], (f, g) failure fragments of unloading test, and (h) the face of the test tunnel [39].

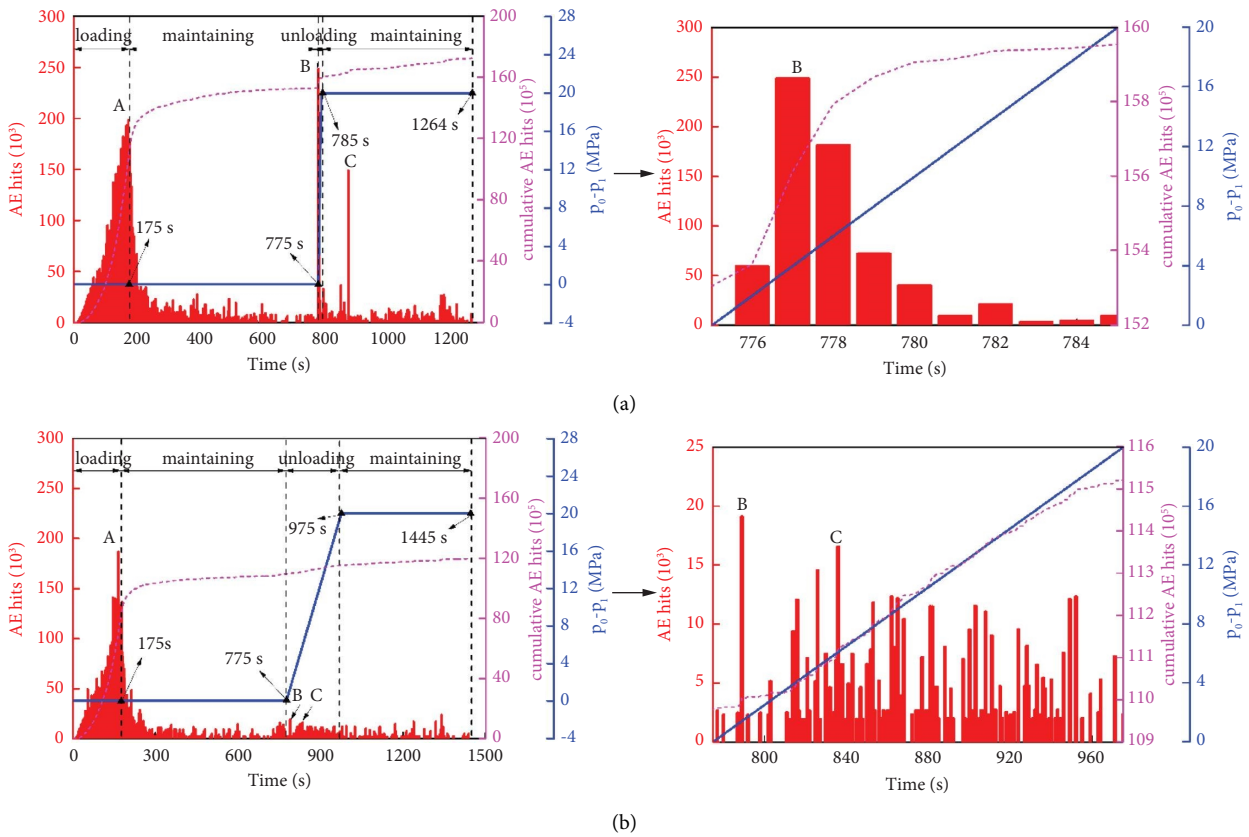

Figure 15: Evolution of AE hits in a whole tests process for specimens with the unloading rates of (a) 2 MPa/s and (b) 0.1 MPa/s.

circumstances of a persistent stress increasing and nearly reached the peak at the end of loading (point A in Figures 15(a) and 15(b)). The original microcracks and microholes in the specimen were closed due to the loading adjustment, which was also observed from true-triaxial unloading tests [41]. (b) In the maintenance stage, the AE hits decreased rapidly and remained at a low level, as the density of AE hits descended. (c) In the unloading stage and maintenance stage after unloading, AE hits sharply increased to a certain high point B, and then decreased exponentially, as shown in Figure 15. Apparently, at unloading rate of 2 MPa/s, AE hit of point B was approximately 249×10^3 (Figure 15(a)). It was approximately 19×10^3 (Figure 15(b)) at the unloading rate of 0.1 MPa/s, far less than that of 2 MPa/s. Subsequently, the next relative high point C appeared after several discontinuous quiet periods at 871 s (maintenance stage after unloading), and had a value of approximately 149×10^3 (Figure 15(a)) at the unloading rate of 2 MPa/s. However, when the unloading rate was 0.1 MPa/s, it was approximately 17×10^3 (Figure 15(b)) at 836 s (unloading stage). Finally, the AE hits dropped intensively and showed a slow climbing trend. This means that there is still an active period of AE after unloading stage under rapid unloading condition, which is the rapid development period of the crack. Note that AE hits shows that AE events slightly lag behind strain rate changes, but their trend is consistent.

The frequency domain information is obtained by performing a fast Fourier transformation (FFT) method on the AE waveform data during the whole testing process. Figure 16 shows the amplitudes and peak frequency distribution of two unloading rates, which can be used to provide additional quantitative information about the unloading testing. As presented in Figure 16, AE signals were characterized by a dense frequency-amplitude distribution. It is seen that the amplitude and peak frequency were distributed in a certain range (65–120 dB, 0–400 kHz) during the testing process under different unloading rates. High unloading rate led to higher amplitudes and wider frequency band. It is clear that the amplitude value of the low frequency (<200 kHz) is much larger than that of the high frequency (>200 kHz) from the frequency-amplitude distribution point in Figure 16. AE events occurred primarily in two main frequency bands below 200 kHz, including a range of 40–100 kHz and another range of approximately 140–190 kHz.

Figure 17 shows the damage evolution in the four stages with the unloading rates of 2 MPa/s and 0.1 MPa/s under initial confining stress of 20 MPa. (a) In the initial loading stage, the damage gradually increased and the growth rate quickened. (b) In the maintenance stage, the damage increased slowly and the growth rate decreased. (c) In the unloading stage, the damage grew faster. The damage growth rate at a discharge rate of 2 MPa/s was higher than that at a discharge rate of 0.1 MPa/s. This phenomenon was more pronounced under the action of high-altitude stress. (d) In the maintenance stage after unloading, the damage and the ratio of the damage continue to increase. The increase of the initial confining stress led to a high damage growth rate at this stage. As a result, the amount of damage generated at this stage accounted for more than 55% of the total damage under rapid unloading rates. In general, the damage evolution law of two unloading rates was basically the same under the condition of relatively low local stress (20 MPa), and there was no destruction after unloading (Figures 14(a) and 14(b)).

4. Mechanisms of Fracture: Insights from Strain Rate and AE

4.1. Insight from Strain Rate. Strain rate can directly reflect the speed of deformation per unit time and indirectly reflect the friction between particles in the specimen and the intensity of spatial relative position change [42]. The radial strain rate shows disparate characteristics under two unloading rates. The larger the unloading rate was, the larger the radial strain rate was. At the initial unloading, the deviatoric stress was small, and the initial radial strain rate of the two unloading rates was also small. As the deviatoric stress increased, the original crack was expanded, and the friction effect of particle was strengthened. When the unloading speed was fast, large microcracks instead of small microcracks were produced in a short time and large relative displacement of particles appeared, which resulted in severe rubbing. When the critical failure value is reached, the particles were thrown. Subsequently, the increment of displacement between large cracks decreased, and small cracks gradually formed. When the unloading rate was low, a long time was used to conduct a stress adjustment, and microcracks continued to initiate, interact, and propagate. As a result, when the unloading rate was 2 MPa/s, the peak value of the strain rate appeared earlier and the value was larger. However, when the unloading rate was 0.1 MPa/s, the peak value of the strain rate appeared later and the value was smaller.

4.2. Insight from AE Characteristics. During the testing process, a large number of AE signals will be generated along with the vibration, compression, shear, and breakage of the surrounding rock. AE signals are quite sensitive to material cracks and damage events and can reflect the inner damage inside the specimen [41], making up for the shortcomings of other monitoring ways. The number of AE hits is correlated with the number of cracks in the specimen [43]. Furthermore, studies have shown that AE hits not only can reflect the characteristics of rock materials in peak phase, but also can reflect that of the initial compression and elastic stage well [44]. Hence, the AE hits can be used to investigate the cracking activities during unloading process.

Figure 18 shows the evolution characteristics of damage during the whole testing process under initial confining stress of 30 MPa. It can be seen from Figures 17 and 18 that the law of damage variable changes will be affected by the confining stress and unloading rate. Obviously, under the same stress conditions, the unloading stage produced a greater amount of damage when the unloading speed was faster. At the same unloading rate, the greater the ground stress, the greater the amount of damage generated during the unloading stage.

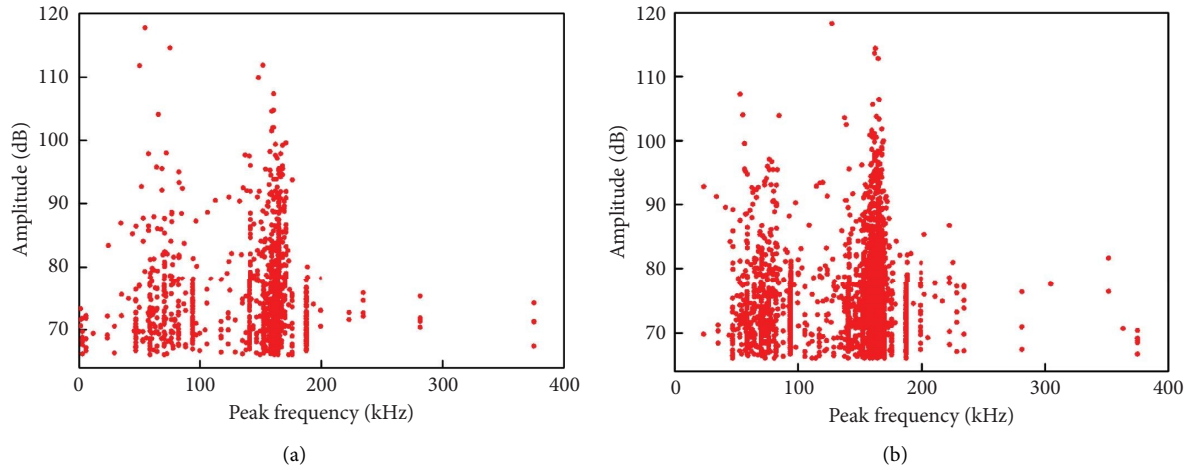

Figure 16: Peak frequency-amplitude distributions for specimens with the unloading rates of (a) 2 MPa/s and (b) 0.1 MPa/s.

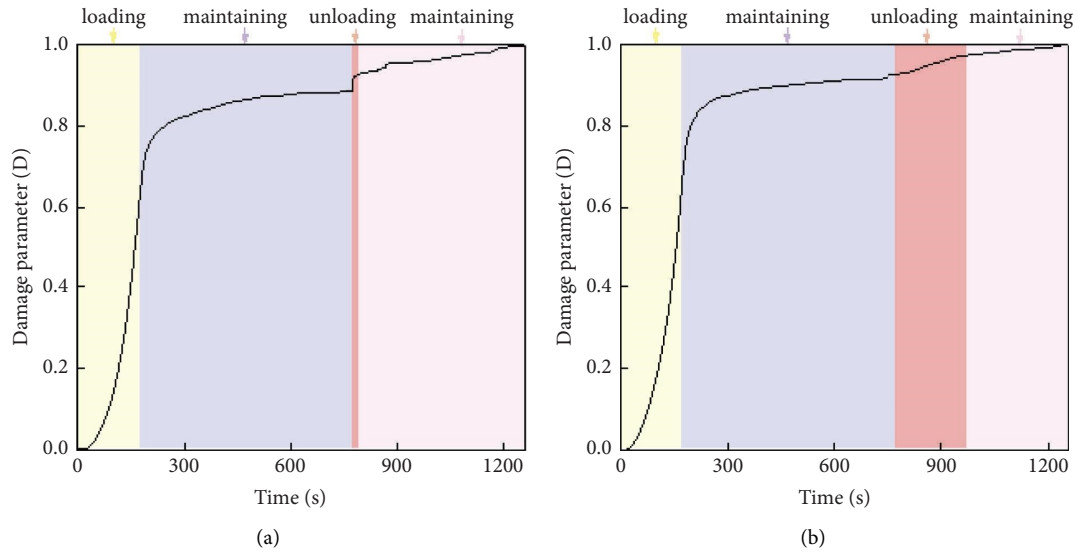

Figure 17: (a, b) The evolution characteristics of damage in a whole tests process for specimens with the unloading rates of 2 MPa/s and 0.1 MPa/s under initial confining stress of 20 MPa.

Figure 19 shows the variation curves of cumulative AE hits under confining stress conditions of 30 MPa. Although the initial confining stresses were different, the evolution characteristics of AE hits were similar for the same unloading rates. The cumulative AE hits at confining stress of 30 MPa were significantly higher than that at confining stress of 20 MPa. When the axial, internal, and external loading reached 20 MPa, the curves of four specimens coincided, and the cumulative AE hits were almost the same (Figure 19(a)). It is indicated that the specimens were characterized by low dispersion degree and high consistency.

Figure 19(b) shows the increment of AE hits at unloading stage. AE hits experienced a nearly steady increase until a sharply increase period, followed by a steady increase when the unloading rate was 2 MPa/s. However, AE hits maintained a constant rise during the unloading process, when the unloading rate was 0.1 MPa/s. When the confining stress was 20 MPa, the increments of cumulate AE hits for two unloading rates in this stage were almost the same, though the slope of cumulative AE hits curve were different clearly. However, there was a great difference, when the confining stress was 30 MPa. This reveals that under high in situ stress condition, the adjustment of unloading rate has a significant effect on the number of internal cracks in the specimen.

After unloading, as shown in Figure 19(a), cumulative AE hits growth rate was slightly lower than the unloading stage at first, and then continued to increase rapidly. This phenomenon was more obvious at the initial confining stress of 30 MPa. Especially under the condition of the unloading rate of 2 MPa/s, cumulative AE hits after unloading testing was even increased to 2500×10^5. Damage and failure degree of corresponding specimen was also more serious (Figure 14(c)). This indicates that microcracks in the

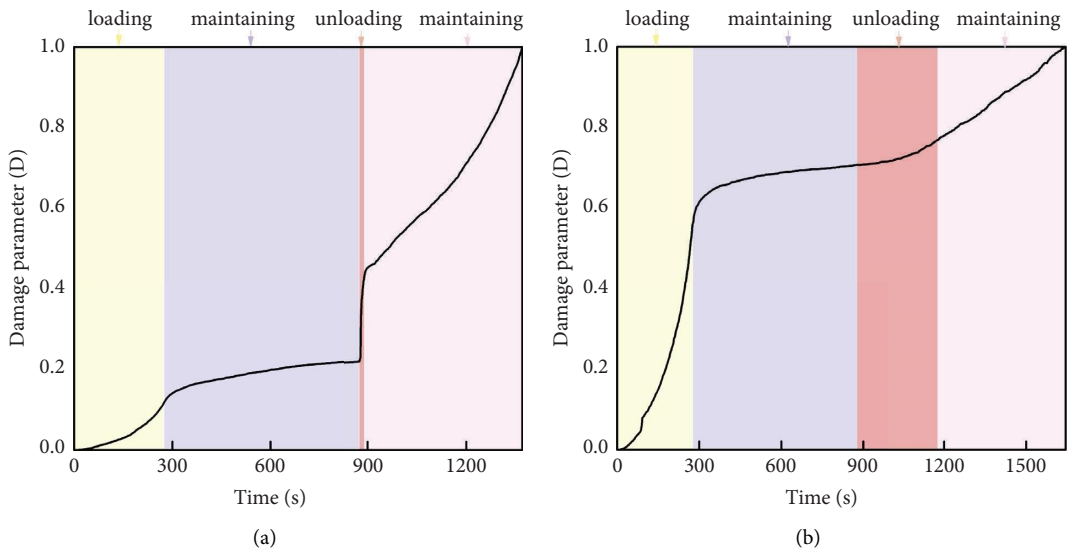

Figure 18: (a, b) The evolution characteristics of damage during the whole testing for specimens with the unloading rates of 2 MPa/s and 0.1 MPa/s under initial confining stress of 30 MPa.

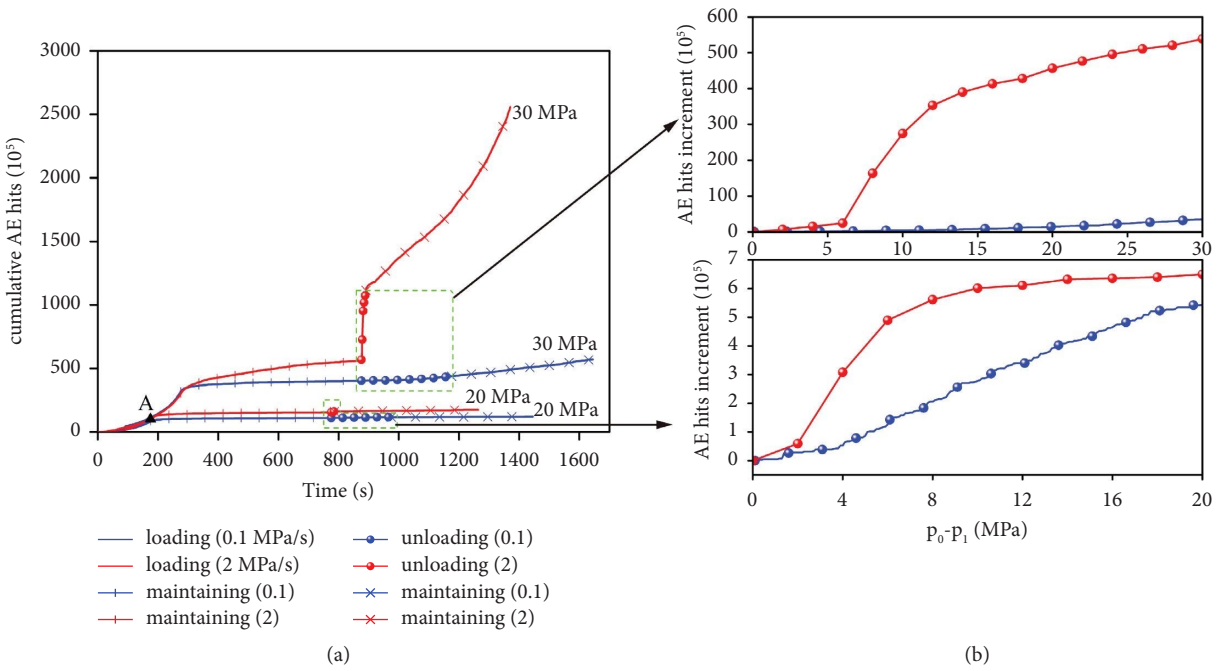

Figure 19: AE signals: (a) AE hits signals during the whole testing process for specimens with the unloading rates of 2 MPa/s and 0.1 MPa/s under initial confining stress of 20 MPa and 30 MPa and (b) AE hits signals for unloading stage with the unloading rates of 2 MPa/s and 0.1 MPa/s under initial confining stress of 20 MPa and 30 MPa.

specimen continued to generate, propagate, interact, and coalesce into macrofractures, which caused the deformation of the surrounding rock. This may be explained why rockburst would occur in a period of time after unloading at a relatively fast unloading rate, which have been observed by numerical simulation [45] and laboratory experiments [41, 46].

Under the same testing conditions, the strain energy stored in specimens is same basically before failure under the same confining stress. When the initial confining stress climbs to 20 MPa, the strain energy stored in the sample is lower. During the unloading process, the radial expansion consumes part of the strain energy, and the accumulated strain energy in the wall rock is not enough to produce damage. When the initial confining stress increases to 30 MPa, the accumulated energy increases. Under the condition of rapid unloading, the stress adjustment is not sufficient and the elastic strain energy accumulated in the specimen is not fully released in time. After unloading, under the continuous action of axial and external stress, the surrounding rock continues to be affected by the excavation

unloading effect. The continuous formation and convergence of fractures lead to the decrease of energy storage capacity. Spalling, ejection, and throwing will occur when the residual elastic strain energy is greater than the kinetic energy needed for rock blocks to leave the matrix. In contrast, when the unloading rate is slow, the strain energy release time increases, and cracks develop gradually.

Although the testing system cannot achieve a three-dimensional unequal stress state really, this testing has obtained interesting research results under special (three--way equal) stress states, which are of great significance for continuing to study the mechanical response and AE response of excavation surrounding rock under different environmental and coupling conditions. The excavation unloading in deep excavation belongs to the gradual unloading in stages, which is difficult to simulate in the laboratory [47]. At present, few experimental systems can simulate the step-by-step excavation of roadway in three-dimensional stress state. Further research is expected to improve the function of the system to be closer to the actual stress environment.

5. Conclusions

A new type of tunnel excavation unloading model testing system was successfully constructed, and the deformation, failure response, and AE behavior of PHTWC cement mortar specimens at different unloading rates were preliminarily studied by combining AE system and strain monitoring system. According to the testing results, the following conclusions can be drawn.

Tensile deformation of cement mortar surrounding rock specimen caused by unloading is greatly affected by unloading rate. The total radial deformation increases with the increase of the unloading rate. The amount of deformation behind the face is significantly higher than that in front of the face, and the radial strain increases with the increase of the distance from the surface within the range affected by unloading. Furthermore, the surrounding rock of the inner hollow free sidewalls might be more susceptible to the unloading effect.

The unloading rate has a little effect on the radial strain rate of the surrounding rock in front of the face, but has a substantial effect on the radial strain rate behind the excavation surface. When the unloading rate is 2 MPa/s, the fitting curves of strain rate can be divided into two sections. The strain rate increases linearly and reaches a peak when the stress is relieved to 30% of the initial confining stress, and then decreases exponentially and stabilizes around 0 value. At the unloading rate of 0.1 MPa/s, the fitting curves of the strain rate can be divided into three sections. The strain rate increases linearly, then exponentially reaches its peak when the stress is discharged to 94% of initial confining stress, and finally decreases exponentially and stabilizes around 0 value. The peak value of strain rate at the unloading rate of 2 MPa/s is much higher than that at the unloading rate of 0.1 MPa/s.

The severity of the failure range increases with the increase of unloading speed. Surrounding rock expanded to the inner hollow, leading to the reduction of the hole diameter of the specimen after the whole unloading test. A large number of rock slices are generated at the opening curved free surface and then fell off, whose morphology is similar to the rock blocks that fell off after caving failure and rock burst in situ field.

From AE monitoring results and testing results, it can be seen that the increasing initial stress and unloading rate will aggravate the damage degree of the specimen. Relatively high bias stresses can trigger the failure behavior of rock specimens, and the damage is prone to appear on the inner surface of the specimens under high confining pressure. AE hits indicate that the faster the unloading rate is, the more severe the damage degree of the specimen is. Under high in situ stress condition, the adjustment of unloading rate has a significant effect on the damage accumulation and crack development in the specimen.

Symbols

σ_z: Axial stress
σ_0: External confining stress
σ_1: Internal confining stress
ε_r: Radial strain
$\dot{\varepsilon}_r$: Radial strain rate
E: Young's modulus
ν: Poisson's ratio
ρ: Density.

Abbreviations

AE: Acoustic emission
PHTWC: Partial hollow thick-walled cylinder
TWC: Thick-walled cylinder
CS: Compressive strength.

Data Availability

The data used to support the findings of this study are available from the corresponding author upon request.

Conflicts of Interest

The authors declare that they have no conflicts of interest.

Acknowledgments

This research was financially supported by the Fundamental Research Funds for the Central Universities (no. ZY20230208) and the National Natural Science Foundation of China (nos. 51574247 and U2034205).

References

[1] Q. H. Qian and X. P. Zhou, "Failure behaviors and rock deformation during excavation of underground cavern group for jinping I hydropower station," *Rock Mechanics and Rock Engineering*, vol. 51, no. 8, pp. 2639–2651, 2018.

[2] C. S. Wang, H. W. Zhou, R. Wang, Z. H. Wang, S. S. He, and J. F. Liu, "Failure characteristics of Beishan granite under unloading confining pressures," *Chinese Journal of Geotechnical Engineering*, vol. 41, no. 2, pp. 329–337, 2019.

[3] W. C. Zhu, S. Li, L. L. Niu, K. Liu, and T. Xu, "Experimental and numerical study on stress relaxation of sandstones disturbed by dynamic loading," *Rock Mechanics and Rock Engineering*, vol. 49, no. 10, pp. 3963–3982, 2016.

[4] C. Wang, "The optimal support intensity for coal mine roadway tunnels in soft rocks," *International Journal of Rock Mechanics and Mining Sciences*, vol. 37, no. 7, pp. 1155–1160, 2000.

[5] M. Abdel-Meguid, R. K. Rowe, and K. Y. Lo, "Three-dimensional analysis of unlined tunnels in rock subjected to high horizontal stress," *Canadian Geotechnical Journal*, vol. 40, no. 6, pp. 1208–1224, 2003.

[6] S. C. Wu, X. J. Geng, Y. T. Gao, G. J. Zhao, J. Li, and Q. Yan, "A study of the longitudinal deformation of tunnels based on the generalized Hoek-Brown failure criterion," *Rock and Soil Mechanics*, vol. 36, no. 4, pp. 946–952+987, 2015.

[7] N. Vlachopoulos and M. S. Diederichs, "Improved longitudinal displacement profiles for convergence confinement analysis of deep tunnels," *Rock Mechanics and Rock Engineering*, vol. 42, no. 2, pp. 131–146, 2009.

[8] Z. Guan, Y. Jiang, and Y. Tanabashi, "Rheological parameter estimation for the prediction of long-term deformations in conventional tunnelling," *Tunnelling and Underground Space Technology*, vol. 24, no. 3, pp. 250–259, 2009.

[9] M. Sharifzadeh, A. Tarifard, and M. A. Moridi, "Time-dependent behavior of tunnel lining in weak rock mass based on displacement back analysis method," *Tunnelling and Underground Space Technology*, vol. 38, pp. 348–356, 2013.

[10] E. Boidy, A. Bouvard, and F. Pellet, "Back analysis of time-dependent behaviour of a test gallery in claystone," *Tunnelling and Underground Space Technology*, vol. 17, no. 4, pp. 415–424, 2002.

[11] N. C. Gay, "Fracture growth around openings in thick-walled cylinders of rock subjected to hydrostatic compression," *International Journal of Rock Mechanics and Mining Sciences and Geomechanics Abstracts*, vol. 10, no. 3, pp. 209–233, 1973.

[12] M. I. Alsayed, "Utilising the Hoek triaxial cell for multiaxial testing of hollow rock cylinders," *International Journal of Rock Mechanics and Mining Sciences*, vol. 39, no. 3, pp. 355–366, 2002.

[13] M. S. Diederichs, "The 2003 Canadian Geotechnical Colloquium: mechanistic interpretation and practical application of damage and spalling prediction criteria for deep tunnelling," *Canadian Geotechnical Journal*, vol. 44, no. 9, pp. 1082–1116, 2007.

[14] Q. H. Wu, X. B. Li, M. Tao, F. J. Zhao, L. Weng, and L. J. Dong, "Conventional triaxial compression on hollow cylinders of sandstone with various fillings: relationship of surrounding rock with support," *J. Cent.South Univ*, vol. 25, no. 8, pp. 1976–1986, 2018.

[15] S. F. Wang, X. B. Li, K. Du, S. Y. Wang, and M. Tao, "Experimental study of the triaxial strength properties of hollow cylindrical granite specimens under coupled external and internal confining stresses," *Rock Mechanics and Rock Engineering*, vol. 51, no. 7, pp. 2015–2031, 2018.

[16] H. Q. Zhang, H. G. Liu, Y. N. He, and L. J. Han, "Unloading experiment and rock strength failure of rock thick-walled cylinders under triaxial compression," *Journal of University of Science and Technology Beijing*, vol. 33, pp. 800–805, 2011.

[17] Q. H. Wu, X. B. Li, F. J. Zhao, M. Tao, L. J. Dong, and L. Chen, "Failure characteristics of hollow cylindrical specimens of limestone under hole pressure unloading," *Chinese Journal of Rock Mechanics and Engineering*, vol. 36, no. 6, pp. 1424–1433, 2017.

[18] V. Labiouse, C. Sauthier, and S. You, "Hollow cylinder simulation experiments of galleries in boom clay formation," *Rock Mechanics and Rock Engineering*, vol. 47, no. 1, pp. 43–55, 2014.

[19] V. Labiouse and T. Vietor, "Laboratory and in situ simulation tests of the excavation damaged zone around galleries in Opalinus clay," *Rock Mechanics and Rock Engineering*, vol. 47, no. 1, pp. 57–70, 2014.

[20] F. Santarelli and E. T. Brown, "Failure of three sedimentary rocks in triaxial and hollow cylinder compression tests," *International Journal of Rock Mechanics and Mining Sciences and Geomechanics Abstracts*, vol. 26, no. 5, pp. 401–413, 1989.

[21] D. H. Lee, C. H. Juang, H. M. Lin, and S. H. Yeh, "Mechanical behavior of Tien-Liao mudstone in hollow cylinder tests," *Canadian Geotechnical Journal*, vol. 39, no. 3, pp. 744–756, 2002.

[22] E. R. Hoskins, "The failure of thick-walled hollow cylinders of isotropic rock," *International Journal of Rock Mechanics and Mining Sciences and Geomechanics Abstracts*, vol. 6, no. 1, pp. 99–125, 1969.

[23] Q. L. Wu, A. Z. Lü, Y. T. Gao, S. C. Wu, and N. Zhang, "Stress analytical solution for plane problem of a double-layered thick-walled cylinder subjected to a type of non-uniform distributed pressure," *J. Cent. South Univ*, vol. 21, no. 5, pp. 2074–2082, 2014.

[24] J. R. Lu, "Mechanism of zonal disintegration within surrounding rock of deep tunnel based on 3D analytical model of thick-walled cylinder," *Rock and Soil Mechanics*, vol. 35, no. 9, pp. 2673–2684, 2014.

[25] E. T. Brown, J. A. Hudson, M. P. Hardy, and C. Fairhurst, "Controlled failure of hollow rock cylinders in uniaxial compression," *Rock Mechanics Felsmechanik Mecanique des Roches*, vol. 4, pp. 1–24, 1972.

[26] Y. B. Zhang, X. L. Yao, P. Liang et al., "Fracture evolution and localization effect of damage in rock based on wave velocity imaging technology," *J. Cent. South Univ*, vol. 28, no. 9, pp. 2752–2769, 2021.

[27] L. J. Dong, Q. Tao, and Q. C. Hu, "Influence of temperature on acoustic emission source location accuracy in underground structure," *Transactions of Nonferrous Metals Society of China*, vol. 31, no. 8, pp. 2468–2478, 2021.

[28] L. J. Dong, Z. W. Pei, X. Xie, Y. Zhang, and X. H. Yan, "Early identification of abnormal regions in rock-mass using traveltime tomography," *Engineering*, vol. 22, pp. 191–200, 2023.

[29] L. J. Dong, X. J. Tong, and J. Ma, "Quantitative investigation of tomographic effects in abnormal regions of complex structures," *Engineering*, vol. 7, no. 7, pp. 1011–1022, 2021.

[30] L. J. Dong, Q. Tao, Q. C. Hu et al., "Acoustic emission source location method and experimental verification for structures containing unknown empty areas," *International Journal of Mining Science and Technology*, vol. 32, no. 3, pp. 487–497, 2022.

[31] G. Y. Hou, X. R. Li, Z. D. Zhang, H. Y. Liang, and J. C. Zhang, "Experimental system for simulating excavation unloading process of rock around roadway by using small cylindrical hollow specimen," *Chinese Journal of Rock Mechanics and Engineering*, vol. 36, no. 9, pp. 2136–2145, 2017.

[32] L. Li, X. Xiao, S. Li, X. Jiao, J. F. Hejtmancik, and Q. Zhang, "Lack of phenotypic effect of triallelic variation in SPATA7 in a family with Leber congenital amaurosis resulting from CRB1 mutations," *Molecular Vision*, vol. 17, pp. 3326–3332, 2011.

[33] A. V. Dyskin, L. N. Germanovich, and K. B. Ustinov, "A 3D model of wing crack growth and interaction," *Engineering Fracture Mechanics*, vol. 63, no. 1, pp. 81–110, 1999.

[34] L. N. Germanovich, R. L. Salganik, V. Dyskin, and K. K. Lee, "Mechanisms of brittle fracture of rock with pre-existing cracks in compression," *Pure and Applied Geophysics PAGEOPH*, vol. 143, no. 1-3, pp. 117–149, 1994.

[35] G. Y. Hou, J. P. Liang, H. Y. Jing et al., "Influence of deviatoric stress on the deformation and damage evolution of surrounding rock under unloading conditions," *Shock and Vibration*, vol. 2020, Article ID 3158209, 14 pages, 2020.

[36] C. D. Martin, "Seventeenth canadian geotechnical colloquium: the effect of cohesion loss and stress path on brittle rock strength," *Canadian Geotechnical Journal*, vol. 34, no. 5, pp. 698–725, 1997.

[37] X. F. Zhao, C. M. Wang, and X. L. Kong, "Analysis of time-space effects of construction behavior of deep soft rock tunnel," *Chinese Journal of Rock Mechanics and Engineering*, vol. 26, no. 2, pp. 404–409, 2007.

[38] C. Martini, R. S. Read, and J. B. Martino, "Observations of brittle failure around a circular test tunnel," *International Journal of Rock Mechanics and Mining Sciences*, vol. 34, no. 7, pp. 1065–1073, 1997.

[39] B. R. Chen, X. T. Feng, H. J. Ming et al., "Evolution law and mechanism of rockbursts in deep tunnel: time delayed rockburst," *Chinese Journal of Rock Mechanics and Engineering*, vol. 1, pp. 561–569, 2012.

[40] X. C. Hu, G. S. Su, G. Y. Chen et al., "Experiment on rockburst process of borehole and its acoustic emission characteristics," *Rock Mechanics and Rock Engineering*, vol. 52, no. 3, pp. 783–802, 2019.

[41] X. G. Zhao, J. Wang, M. Cai et al., "Influence of unloading rate on the strainburst characteristics of Beishan granite under true-triaxial unloading conditions," *Rock Mechanics and Rock Engineering*, vol. 47, no. 2, pp. 467–483, 2014.

[42] X. Gao, S. J. Liu, J. W. Huang, Z. C. Yang, W. F. Mao, and L. X. Wu, "The influence of strain rate on AE characteristics during rock deformation," *Chinese Journal of Rock Mechanics and Engineering*, vol. 37, no. 4, pp. 887–897, 2018.

[43] Z. Moradian, H. H. Einstein, and G. Ballivy, "Detection of cracking levels in brittle rocks by parametric analysis of the acoustic emission signals," *Rock Mechanics and Rock Engineering*, vol. 49, no. 3, pp. 785–800, 2016.

[44] X. Wang, Z. J. Wen, Y. J. Jiang, and H. Huang, "Experimental study on mechanical and acoustic emission characteristics of rock-like material under non-uniformly distributed loads," *Rock Mechanics and Rock Engineering*, vol. 51, no. 3, pp. 729–745, 2018.

[45] X. B. Li, Z. H. Chen, W. Z. Cao, M. Tao, and J. Zhou, "Time-effect properties and mechanisms of marble failure under different unloading rates," *Chinese Journal of Geotechnical Engineering*, vol. 39, no. 9, pp. 1565–1574, 2017.

[46] A. M. Linkov, "Rockbursts and the instability of rock masses," *International Journal of Rock Mechanics and Mining Sciences and Geomechanics Abstracts*, vol. 33, no. 7, pp. 727–732, 1996.

[47] G. Q. Zhu, X. T. Feng, Y. Y. Zhou, Z. W. Li, L. J. Fu, and Y. R. Xiong, "Physical model experimental study on spalling failure around a tunnel in synthetic marble," *Rock Mechanics and Rock Engineering*, vol. 53, no. 2, pp. 909–926, 2020.